J. Fluid Mech. (2001), *vol.* 435, *pp.* 25–54. Printed in the United Kingdom

© 2001 Cambridge University Press

Flow structures and particle deposition patterns in double-bifurcation airway models. Part 1. Air flow fields

By J. K. COMER[1], C. KLEINSTREUER[1]† AND Z. ZHANG[2]

[1]Department of Mechanical and Aerospace Engineering, North Carolina State University, Raleigh, NC 27695-7910, USA

[2]Center for Environmental Medicine and Lung Biology, University of North Carolina, Chapel Hill, NC 27599, USA

(Received 10 May 1999 and in revised form 9 November 2000)

The understanding and quantitative assessment of air flow fields and local micron-particle wall concentrations in tracheobronchial airways are very important for estimating the health risks of inhaled particulate pollutants, developing algebraic transfer functions of global lung deposition models used in dose-response analyses, and/or determining proper drug-aerosol delivery to target sites in the lung. In this paper (Part 1) the theory, model geometries, and air flow results are provided. In a companion paper (Part 2, Comer *et al.* 2001), the history of particle deposition patterns and comparisons with measured data sets are reported. Decoupling of the naturally dilute particle suspension makes it feasible to present the results in two parts.

Considering a Reynolds number range of $500 \leqslant Re_D \leqslant 2000$, it is assumed that the air flow is steady, incompressible and laminar and that the tubular double bifurcations, i.e. Weibel's generations G3–G5, are three-dimensional, rigid, and smooth with rounded as well as sharp carinal ridges for symmetric planar, and just rounded carinas for 90° non-planar configurations. The employed finite-volume code CFX (AEA Technology) and its user-enhanced FORTRAN programs were validated with experimental velocity data points for a single bifurcation. The resulting air flow structures are analysed for relatively low ($Re_D = 500$) and high ($Re_D = 2000$) Reynolds numbers. Sequential pressure drops due to viscous effects were calculated and compared, extending a method proposed by Pedley *et al.* (1977). Such detailed results for bifurcating lung airways are most useful in the development of global algebraic lung models.

1. Introduction

The respiratory airways can be approximated as a network of repeatedly bifurcating tubes with progressively decreasing dimensions and flow rates (Weibel 1963; Hammersely & Olson 1992; Phillips & Kaye 1997). Inhaled particles, e.g. $1 < d_p < 10\,\mu\text{m}$, are deposited primarily by inertial impaction, especially in the relatively large tracheobronchial airways (Gerrity *et al.* 1979; Kim *et al.* 1983). Detailed deposition characteristics of these particulate pollutants are of great importance because they have been linked to lung diseases such as bronchiole inflammation, epithelial tissue injuries and bronchial tumours, especially in susceptible population groups (Fox

† Author to whom correspondence should be addressed: e-mail ck@eos.ncsu.edu

https://doi.org/10.1017/S0022112001003809 Published online by Cambridge University Press

1993). Furthermore, detailed computational analyses of multi-branch airways assist in the development of comprehensive lung models as well as optimal drug delivery systems. Specifically, the complexity of the lung, rendering it at present inaccessible to direct numerical (or experimental) simulations, requires segmental algebraic particle deposition functions in order to develop easy-to-use global lung deposition models for exposure-dose relationship and subsequently for dose-effect analyses. Once critical target areas inside the respiratory airways have been identified for certain groups of patients, therapeutic drug delivery systems can be developed.

Although numerous experimental and numerical studies exist which address selected aspects of air flow and micron-particle deposition in lung segments, realism was often oversimplified where single bifurcations and/or simplistic geometric constructions did not reveal the aerodynamic causes of certain particle deposition patterns. One of the earliest contributions, Schroter & Sudlow (1969), provided a few velocity profiles and flow patterns for bifurcating geometries using hot-wire probes and also smoke tracers. They justified the commonly employed assumptions of steady air flow, rigid walls, and smooth tubular surfaces based on Reynolds number and Womersley parameter arguments. They also showed the flow in bifurcating geometries at higher Reynolds numbers (i.e. $Re_D = 1090$, where Re_D is based on tube diameter D) possessed the characteristic double-peak axial velocity profile in the plane of bifurcation and the characteristic M-shaped profile in the plane perpendicular to the bifurcation. Snyder & Olson (1989) investigated experimentally the suppression of flow separation in pulmonary bifurcations in order to explain the surprisingly effective airway ventilation in the human lung. Gatlin *et al.* (1995) modelled the fluid flow in symmetric 'physiologically correct' bifurcations for both steady and oscillating flow at Reynolds numbers of $Re_D = 500$ and 160 respectively. Later, this model was used for experimental studies of the fluid flow field by Farag *et al.* (1998). The experimental study of Zhao & Lieber (1994) and the numerical study of Zhao, Brunskill & Lieber (1997) modelled flow in idealized bifurcation geometries for inlet Reynolds numbers ranging from 500 to 2000. The geometry in these studies was chosen for ease of replication and to allow smooth transition from the single parent tube to the two daughter tubes (i.e. a constant cross-sectional area was maintained throughout the bifurcation transition region). Although this geometry lacked anatomical details of human bronchial airway structure, we selected this geometry for model validation (see § 3.1) since it could be reliably reproduced.

The number of studies on the double-bifurcation models of interest here is extremely small. The classical paper of Schroter & Sudlow (1969) mentioned above gives a brief description of the flow profiles at three locations in the first and second bifurcation daughter tubes. However, owing to the differences in bifurcation angle, carinal curvature, and Reynolds number, it is difficult to compare these results for the second bifurcation to those of the current system. Also, no detailed measurements are reported in the vicinity of the bifurcation, which is of key interest in the current study. In continuation of their work, Pedley, Schroter & Sudlow (1971) focused on the flow field and pressure drop in multi-branch tubes and developed a ratio of the dissipation in a tube downstream of a bifurcation to the dissipation for Poiseuille flow. Such a methodology is most useful in the development of a global algebraic lung model. The recent study of Lee, Goo & Chung (1996) contains a short discussion of the flow field in bifurcating geometries; but their results have to be viewed with caution because they used the same diameter for both parent and daughter tubes, resulting in a rapid increase in the cross-sectional area, and the length of the daughter tubes was terminated at $3D_d$ past the carina, that is, before the flow has become fully

https://doi.org/10.1017/S0022112001003809 Published online by Cambridge University Press

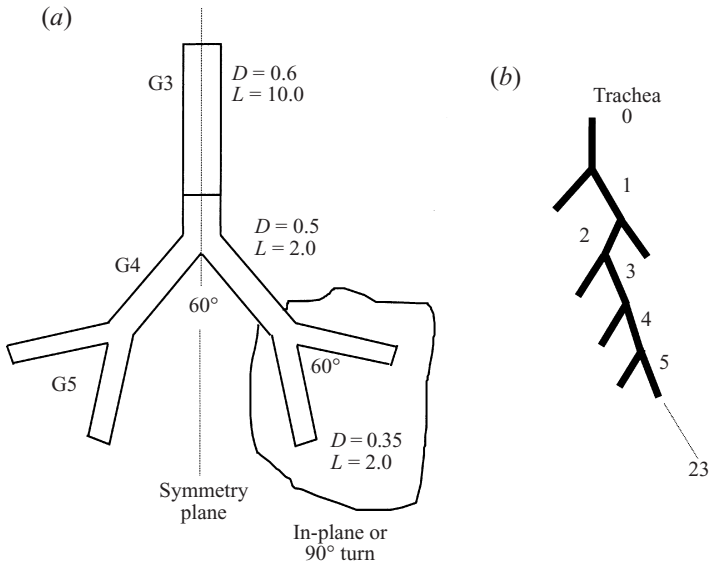


FIGURE 1. Double bifurcation geometries: (*a*) schematics of generations 3, 4 and 5; (*b*) Weibel's lung classification model.

developed, at least at higher Reynolds numbers, i.e. $Re_D \geqslant 500$. Wilquem & Degrez (1997) provided a detailed description of the flow field and pressure drop for steady flow in a double-bifurcation model of the human central airways. However, the study is limited to a two-dimensional configuration and therefore is of little use in describing the complex three-dimensional air flow structures which exist in bifurcating airways.

2. Theory

2.1. *Double-bifurcation geometries*

Two rigid-wall configurations are considered, i.e. a symmetric planar and a 90° non-planar model. Both geometries may be found as generations G3, G4, and G5 employing Weibel's lung classification scheme (Weibel 1963), which is widely used for direct comparison purposes (see figure 1*a*, *b*). These geometries were based on the glass tube models utilized in the experimental study by Kim & Fisher (1999). Owing to the complexity of generating a representative bifurcation model, the CAD package Pro/Engineer was used to generate three-dimensional surface models where the carinal ridges of the planar configurations are either rounded or sharp. The system dimensions are given in figure 2(*a*, *b*) with the associated geometric and kinematic data sets summarized in table 1 and table 2, respectively, for both the planar and non-planar configurations.

In order to avoid turbulence effects, the maximum Reynolds number chosen was $Re_{D_1} = 2000$. The validity of the underlying assumption of steady inspiratory flows in rigid smooth conduits being representative of a portion of the central human airways is discussed in Schroter & Sudlow (1969) and supportive data may be found in Fox (1993).

https://doi.org/10.1017/S0022112001003809 Published online by Cambridge University Press

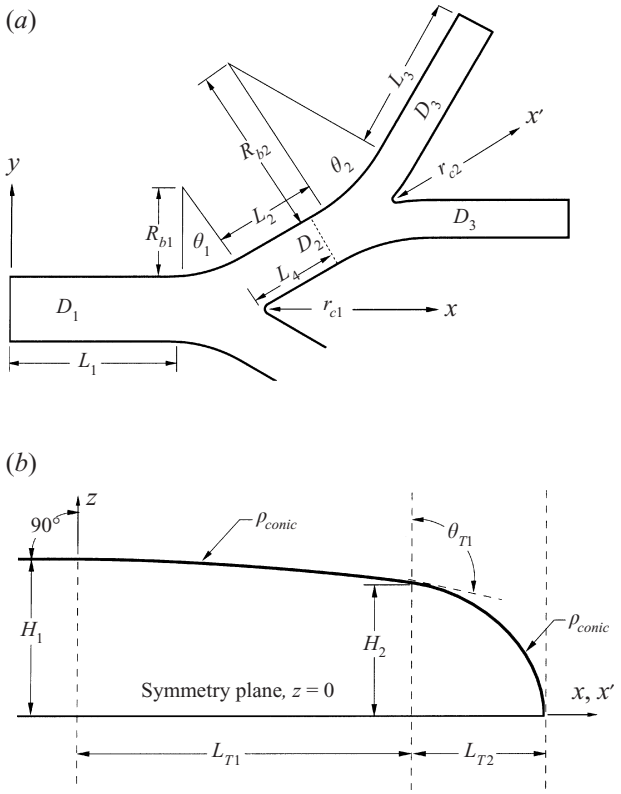


FIGURE 2. Planar geometry: (*a*) symmetry plane ($z = 0$) after Weibel (1963) and Kim & Fisher (1999) and (*b*) bifurcation symmetry plane; see table 1 for data.

2.2. *Governing equations*

The continuity and momentum equations for steady laminar incompressible air flow are given as

$$\nabla \cdot \boldsymbol{v} = 0 \tag{1}$$

and

$$(\boldsymbol{v} \cdot \nabla)\boldsymbol{v} = -\frac{1}{\rho}\nabla p + \nabla \cdot [\nu(\nabla \boldsymbol{v} + (\nabla \boldsymbol{v})^{tr})]. \tag{2}$$

For the steady inhalation phase, a parabolic fluid velocity was specified at the inlet. In the current study, a uniform pressure boundary condition is used for the outlets, which results in symmetric flow about the first carina (i.e. $y = 0$). In studies which are currently in progress, this condition has been modified to measure the effects of the various levels of flow rate asymmetry due to downstream impedances. The boundary conditions for the governing equations include symmetry with respect to the plane of the first bifurcation (i.e. $z = 0$) and no fluid slip at the rigid smooth impermeable walls.

2.3. *Numerical method*

The numerical solution of the fluid flow equations were carried out using a user-enhanced, commercial finite-volume-based program CFX 4.2 (AEA Technology 1997). The numerical program uses a structured, multi-block, body-fitted coordinate discretization scheme. In the present simulation using the CFX program, the SIMPLEC

https://doi.org/10.1017/S0022112001003809 Published online by Cambridge University Press

Bifurcation	First	Second
Parent duct diameter	$D_1 = 0.6$	$D_2 = 0.5$
Daughter duct diameter	$D_2 = 0.5$	$D_3 = 0.35$
Bifurcation radius of curvature	$R_{b1} = 2.7\,D_2$	$R_{b2} = 4.7\,D_3$
Carinal radius of curvature	$r_{c1} = 0.1\,D_2$ or 0	$r_{c2} = 0.1\,D_3$ or 0
Length of ducts	$L_1 = 2.4$	$L_3 = 3.367$
	$L_2 = 0.836$	
Extent of daughter tube to be used in particle deposition calculations	$L_4 = 0.6$	
Bifurcation half-angle	$\theta_1 = 30^\circ$	$\theta_2 = 30^\circ$
Transition region length	$L_{T1} = 0.64$	$L_{T1} = 0.512$
	$L_{T2} = 0.25$	$L_{T2} = 0.18$
Carinal ridge height	$H_1 = 0.6$	$H_1 = 0.5$
	$H_2 = 0.255$	$H_2 = 0.19$
Carinal transition angle	$\theta_{T1} = 98^\circ$	$\theta_{T1} = 105^\circ$
Transition conic dimension	$\rho_{conic} = \sqrt{2}$	$\rho_{conic} = \sqrt{2}$

TABLE 1. Geometric parameters for double-bifurcation models (see figure 2*a*, *b*). All dimensions in centimetres.

Physical state	Sedentary	Light activity	Heavy activity
Respiratory rate	$7.0\,\mathrm{l\,min^{-1}}$	$20.011\,\mathrm{l\,min^{-1}}$	$60\,\mathrm{l\,min^{-1}}$
Time ratio of inspiratory phase (t_{insp}/t_{total})	0.42	0.42	0.42
Mean flow rate during inspiration	$16.7\,\mathrm{l\,min^{-1}}$	$47.7\,\mathrm{l\,min^{-1}}$	$142.9\,\mathrm{l\,min^{-1}}$
Total cross-sectional area ($G = 3$) based on Weibel's model A	$1.97\,\mathrm{cm^2}$	$1.97\,\mathrm{cm^2}$	$1.97\,\mathrm{cm^2}$
Mean inspiratory Re_{D_1}	475	1360	4080

TABLE 2. Respiratory rate data (Martonen *et al.* 1994).

algorithm (Patankar 1983) with under-relaxation was employed to solve the flow equations. The relaxation factor for the velocity is 0.65. All variables, including velocity components and pressure, are located at the centroids of the control volumes. An improved Rhie–Chow interpolation method was employed to obtain the velocity components and pressure on the control volume faces from those at the control volume centres. Hybrid differencing was used to model the convective terms of the transport equations. In order to ensure accurate flow field simulations, especially the secondary velocities, the hybrid scheme has been compared to the third-order QUICK scheme and the resulting differences in terms of relative velocity magnitudes were below 10%. The sets of linearized and discretized equations for all variables were solved using an algebraic multi-grid method (Lonsdale 1993).

A dimensionless approach was adopted for the simulation of the conservation equations. The mean inlet fluid velocity, U, and the fluid density, ρ, were set equal to one, and the fluid dynamic viscosity, μ, was adjusted to achieve the desired fluid Reynolds number, $Re_{D_1} = (\rho D_1 U)/\mu$.

The mesh was generated based on the surface information obtained from the CAD Pro/Engineer models of the experimental glass tube bifurcations mentioned previously (see figure 3*a*–*c*). Utilizing the assumed symmetry condition about the first bifurcation plane, the flow field simulation involved only the upper half of the bifurcation model (i.e. $z \geqslant 0$). The inlet and outlet locations, and the mesh topology

https://doi.org/10.1017/S0022112001003809 Published online by Cambridge University Press

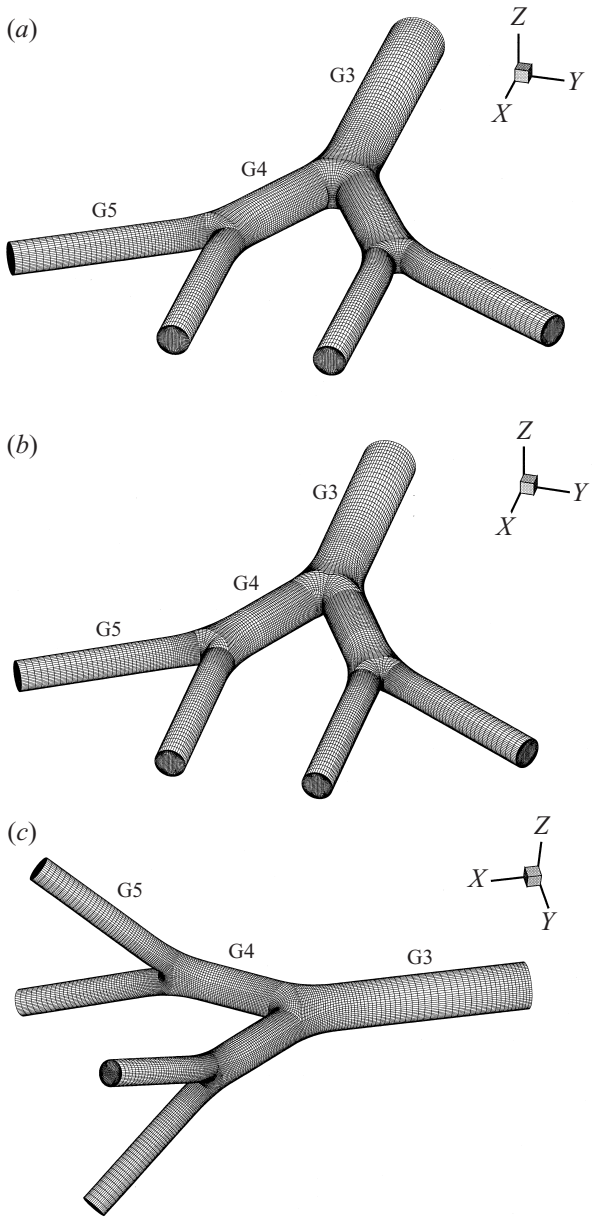


FIGURE 3. Finite volume meshes: (*a*) planar model with rounded carinas; (*b*) planar model with sharp carinas; (*c*) non-planar model with rounded carinas.

were determined by refining the mesh until grid independence of the flow field solution and particle deposition efficiency was achieved. The final mesh size of the planar and 90° non-planar configurations with rounded carinal ridges was 161 000 and 173 000 cells, respectively; for the planar double bifurcation with sharp carinal ridges it was also 161 000 cells. The computations were performed on a Sun Ultra 60 workstation with 512 MB of RAM and two 300 MHz CPUs. The steady-state solution of the flow field was assumed converged when the dimensionless mass residual, (total mass

https://doi.org/10.1017/S0022112001003809 Published online by Cambridge University Press

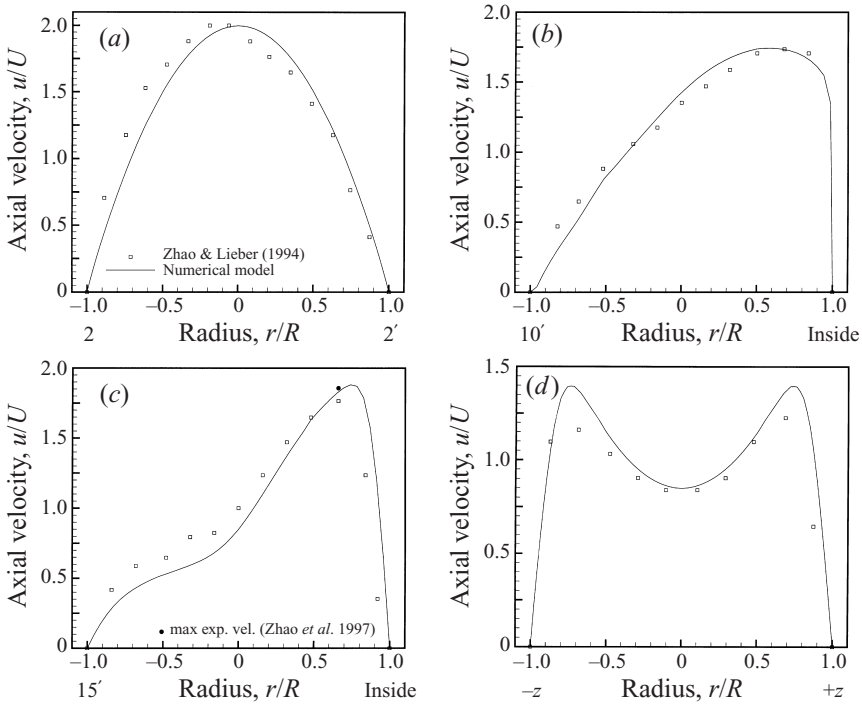


FIGURE 4. Comparison of velocities at $Re_D = 1036$ with Zhao & Lieber (1994): (*a*) cross-section 2–2′; (*b*) cross-section 10′; (*c*) cross-section 15–15′ aligned with bifurcation plane; (*d*) cross-section 15–15′ perpendicular to bifurcation plane.

residual)/(mass flow rate) $< 10^{-3}$. Typical run times for the fluid flow simulations on a single processor was approximately 2.7 hours.

3. Results and discussion

The computer simulation model for air flow has been validated with experimental velocity data of Zhao & Lieber (1994) for symmetric tubular bifurcations. The resulting air velocity fields are discussed for representative low ($Re_{D_1} = 500$) and high ($Re_{D_1} = 2000$) Reynolds number flows in different airway configurations, i.e. planar with rounded or sharp carinal ridges as well as non-planar with rounded carinal ridges. The section concludes with a summary of the basic research findings and possible applications.

3.1. *Model validation*

For two Reynolds numbers, i.e. $Re_D = 518$ and 1036, the measured velocities (Zhao & Lieber 1994) were compared with the computed velocity profiles in a symmetric bifurcation with constant cross-sectional areas, a branching angle of 70°, and a sharp carinal ridge (see figure 1 in Zhao & Lieber 1994). However, only comparisons for $Re_D = 1036$ at three cross-sections 2, 10, and 15 of Zhao & Lieber's model are shown here, while the lower Reynolds number results may be found in Comer (1998). While the upstream axial velocity profile, i.e. cross-section 2 top view in the parent tube, should be perfectly symmetric as predicted, the slightly skewed data points indicate some flow asymmetry, presumably some blockage effect in one of the daughter tubes (see figure 4*a*). At the beginning of the daughter tube, i.e. section 10, the axial velocity

https://doi.org/10.1017/S0022112001003809 Published online by Cambridge University Press

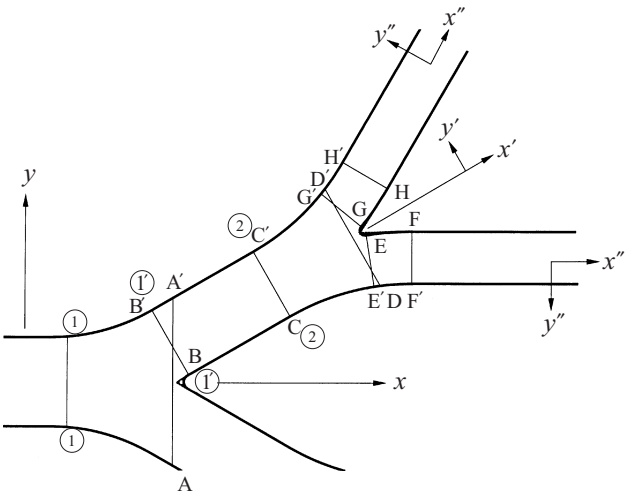


FIGURE 5. Scaled double bifurcation (see figure 2*a*) with coordinate systems and locations of velocity cross-sections (A–A′ to H–H′) as well as the stations (1–1, 1′–1′ and 2–2) for computing energy dissipation rates and pressure drops.

profile is naturally skewed towards the divider wall (see figure 4*b*) and even more pronounced at cross-section 15 (see figure 4*c*). The experimental local maximum velocity as reported in Zhao *et al.* (1997) differs slightly from the one obtained by Zhao & Lieber (1994); however, it compares well with the predicted value. In the transverse plane, i.e. section 15 side view, so-called M-shaped velocity profiles appear due to secondary flow effects, which in turn are dependent on the Reynolds number (see figure 4*d*). No reverse flow was observed in this particular geometry.

3.2. *Velocity fields*

The velocity fields, in terms of mid-plane velocity vector plots and axial velocity contours, are shown for two Reynolds numbers, i.e. $Re_{D_1} = 500$ and 2000, in three configurations (see figure 3*a–c*). The velocity fields at $Re_{D_1} = 500$ and 2000 are shown first for the planar configuration with rounded and sharp ridges and then for the non-planar bifurcation. Figure 5 shows half of the scaled bifurcation geometry with stations A–A′ to H–H′ for which the velocity fields are depicted. An attempt has been made to duplicate faithfully the inside glass tube geometry of Kim & Fisher (1999) with its representative diameters, lengths, cross-sections, wall curvatures, and carinal ridge dimensions (see figure 2*a*, *b* and table 1). These geometric features in conjunction with the fluid inlet condition have to be taken into account when comparing the simulation results to other publications.

3.2.1. *Planar double bifurcation with rounded carinas*

The velocity vector plots in the bifurcation plane, i.e. $z = 0$, show in figures 6(*a*) and 6(*b*) the expected flow fields with subtle differences between the relatively low and high Reynolds number flows. At the higher air flow rate the distinct shear layer along the inside wall after the first carina is thinner and the recirculation zone at the outer wall across from the carinal ridge area is larger when compared to corresponding flow patterns at $Re_{D_1} = 500$. The blockage effect of a vortex on the inside wall downstream of the carina generates, especially at $Re_{D_1} = 2000$ near the second carina, a strong transverse flow component in the second daughter tube. Clearly, the sudden increase

https://doi.org/10.1017/S0022112001003809 Published online by Cambridge University Press

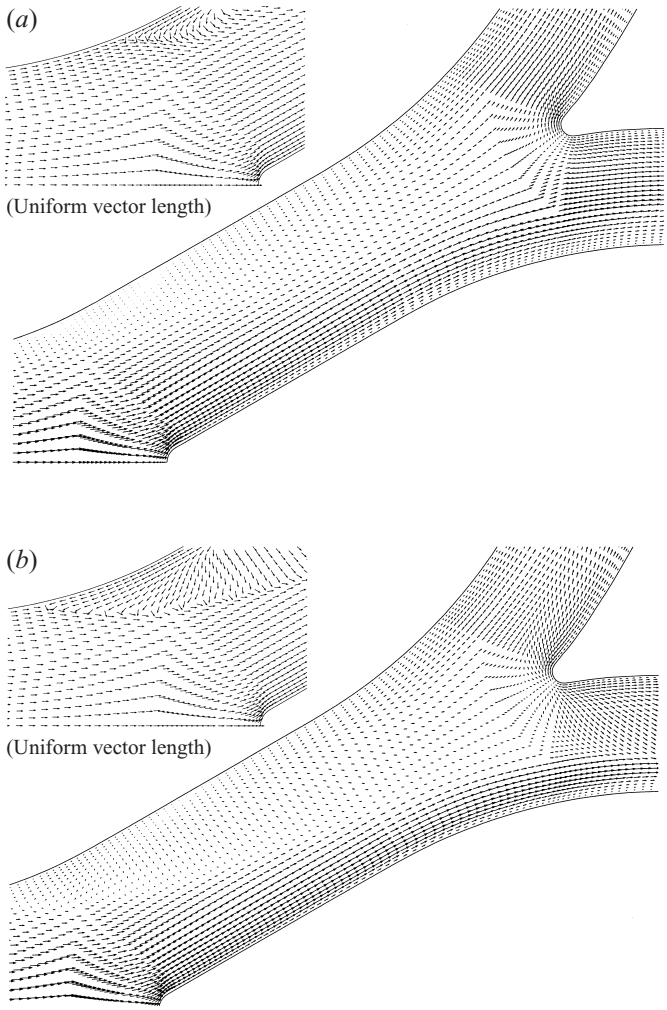


FIGURE 6. Velocity vector plots for planar double bifurcation with rounded carinas: (*a*) inlet Reynolds number $Re_{D_1} = 500$; (*b*) inlet Reynolds number $Re_{D_1} = 2000$.

in flow area at a ratio of 1 : 1.39 at the first bifurcation and the essentially uniform area ratio at the second bifurcation, i.e. 1 : 0.98, in conjunction with the magnitude of the half-angle of each branch as well as the carinal ridge curvature, largely determine the bulk flow features. However, secondary flows, important in aerosol transport and particle wall deposition, are best observed at selected cross-sections.

Axial velocity contours and secondary velocity vectors are given in figure 7(*a*, *b*) for the cross section A–A′, just upstream of the carina. At that station, the flow is adjusting to the geometric transition from a circular parent tube via elliptical cross-sections to the merger toward the two smaller daughter tubes. The contraction of the top and bottom surfaces is clearly evident. Considering the $Re_{D_1} = 500$ case, the axial velocity contours indicate that the bulk stream has split as the fluid moves toward the daughter tubes. This has not yet occurred for the $Re_{D_1} = 2000$ case. This can be attributed to the recirculating flow at the outside of the bifurcation forcing fluid toward the centre. One possible cause is the vortices which exist at the top/bottom

https://doi.org/10.1017/S0022112001003809 Published online by Cambridge University Press

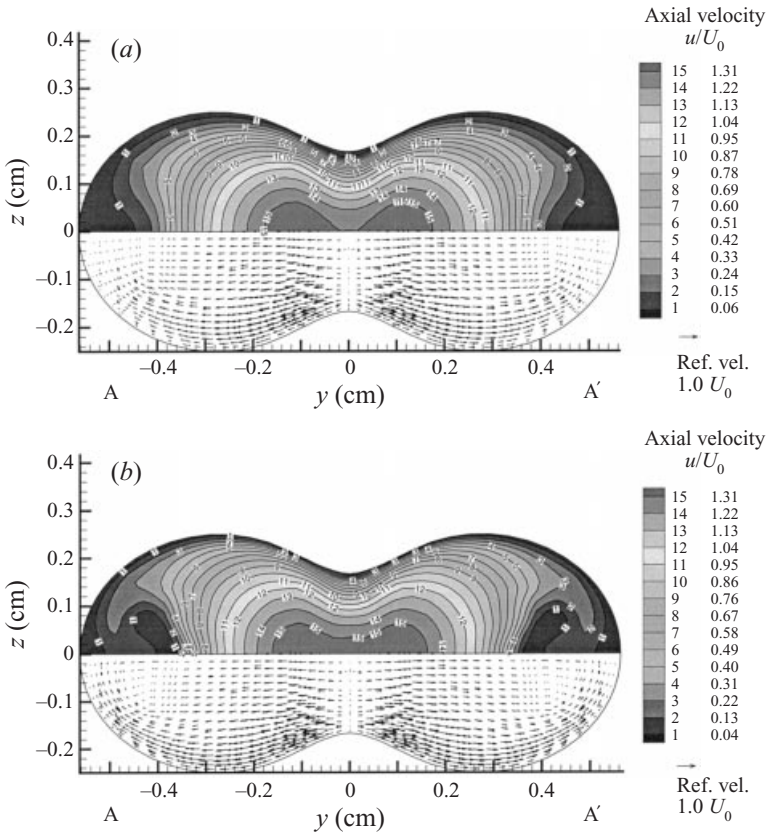


FIGURE 7. Axial velocity contours and secondary velocity vector plots at station A–A′ of planar double bifurcation with rounded carinas for (*a*) $Re_{D_1} = 500$ and (*b*) $Re_{D_1} = 2000$.

of the carinal ridge due to its rounded shape. These vortices laterally wrap around the top/bottom of the geometric transition region.

Figures 8(*a*) and 8(*b*) show the velocity fields in cross-section B–B′ at the beginning of the first daughter tube. For both Reynolds numbers the highest axial velocity is adjacent to the inside wall of the bifurcation. The secondary velocity field exhibits one main vortex which moves the high-speed flow up around the top of the tube toward the outside of the bifurcation and low-speed flow from the outside of the bifurcation along the symmetry plane toward the inside of the bifurcation. For the $Re_{D_1} = 2000$ case, a second co-rotating vortex can be seen at the outside of the bifurcation along the symmetry plane. This secondary vortex may be attributed to flow which wraps around the top/bottom of the bifurcation as mentioned in the discussion for section A–A′. From the axial velocity contours it can be seen that only a single-peak axial profile exists in the plane of the bifurcation and that the characteristic M-profile has yet to appear. This is as expected at the inlet to the first bifurcation. For the higher Reynolds number case, however, the high-speed flow has already begun to wrap around and engulf the slower moving fluid on the outside of the bifurcation.

Figure 9(*a*, *b*) shows the velocity fields in cross-section C–C′ at the beginning of the transition toward the second bifurcation. No additional cross-sections are shown for the first bifurcation since flow in the first (i.e. single) bifurcation daughter tube is well understood and can be interpolated from the results at cross-sections B–B′

https://doi.org/10.1017/S0022112001003809 Published online by Cambridge University Press

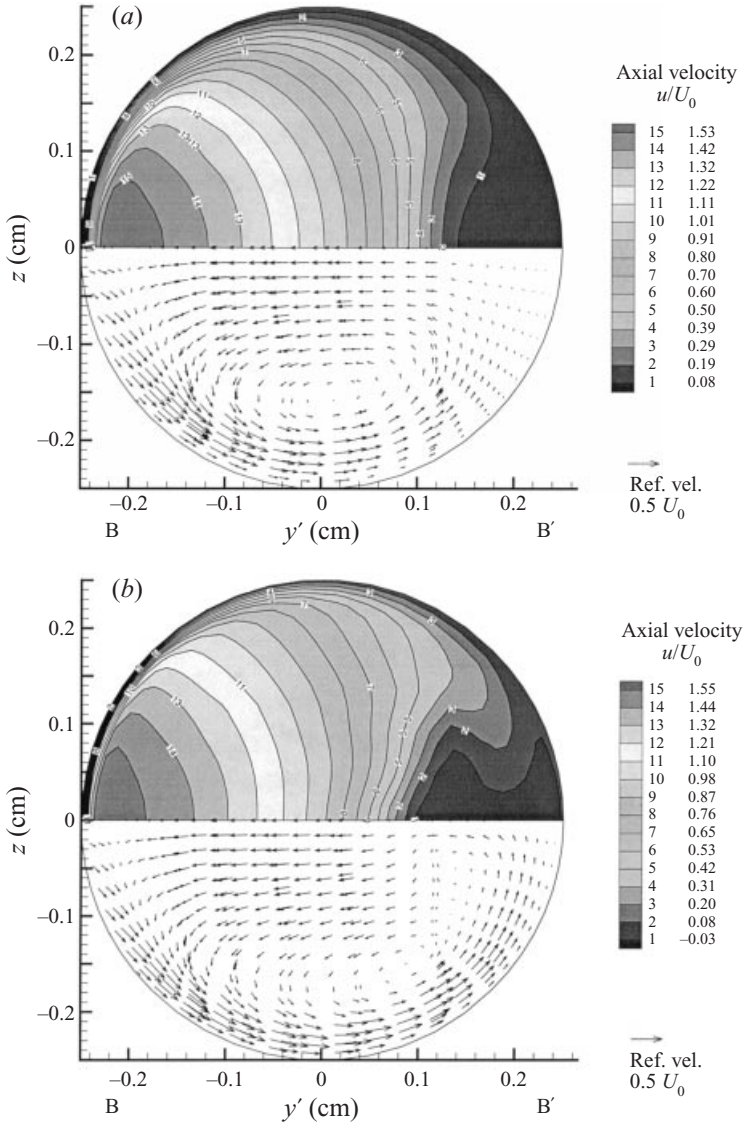


FIGURE 8. As figure 7 but at station B–B′.

and C–C′. The lower Reynolds number flow appears to have shifted further away from the inside wall of the bifurcation and the secondary flow is considerably weaker than the higher Reynolds number flow. From the axial velocity contours it can be seen that at the higher Reynolds number the stronger secondary flow has wrapped the high-velocity flow completely around the outside of the bifurcation engulfing the slower moving fluid which has been pushed to the tube centre. This results in the double-peak axial flow profile at the symmetry plane as described by Schroter & Sudlow (1969). For the lower Reynolds number flow the axial double-peak velocity profile does not appear since the high-speed fluid has not completely wrapped around the tube circumference owing to the weaker secondary flow.

Figure 10(*a*, *b*) shows the velocity fields in cross-section D–D′ just upstream of the second carina. Again, the contraction of the top and bottom surfaces is clearly evident

https://doi.org/10.1017/S0022112001003809 Published online by Cambridge University Press

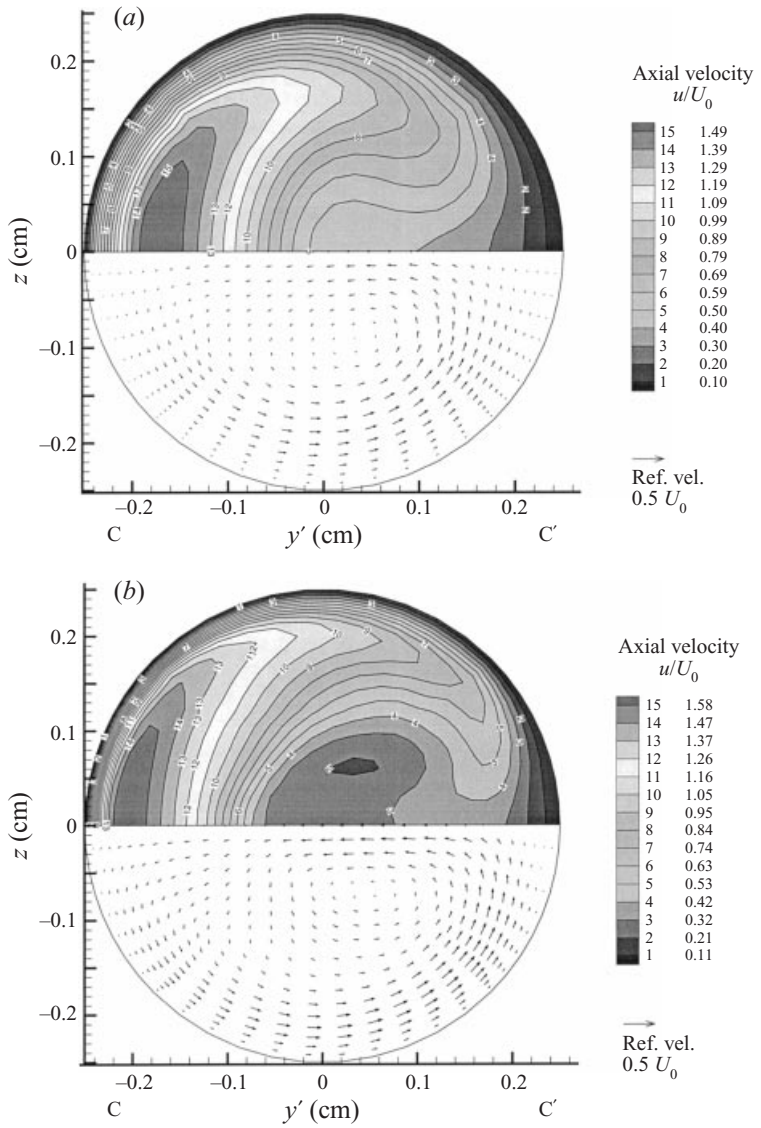


FIGURE 9. As figure 7 but at station C–C′.

and the axial velocity contours for the high Reynolds number flow that were previously shown to be wrapped around the top/bottom of the surfaces have been 'clipped' such that unequal portions of the high-speed flow are directed into each bifurcation. Of course, the largest portion of high-speed flow travels down the inside tube ($-y'$) of the second bifurcation. The high-velocity flow in the inside tube is shifted back toward the centre of the second daughter tube at the low Reynolds number, while for the higher Reynolds number flow it continues to reside closer to the wall. The high-velocity flow which is directed into the outside tube of the second bifurcation initially travels down the tube as two unattached high-velocity streams off-set above and below the symmetry plane. Perhaps the most intriguing aspect of this cross-sectional plot is the extremely low velocity at the carina centre for the low Reynolds number case and

https://doi.org/10.1017/S0022112001003809 Published online by Cambridge University Press

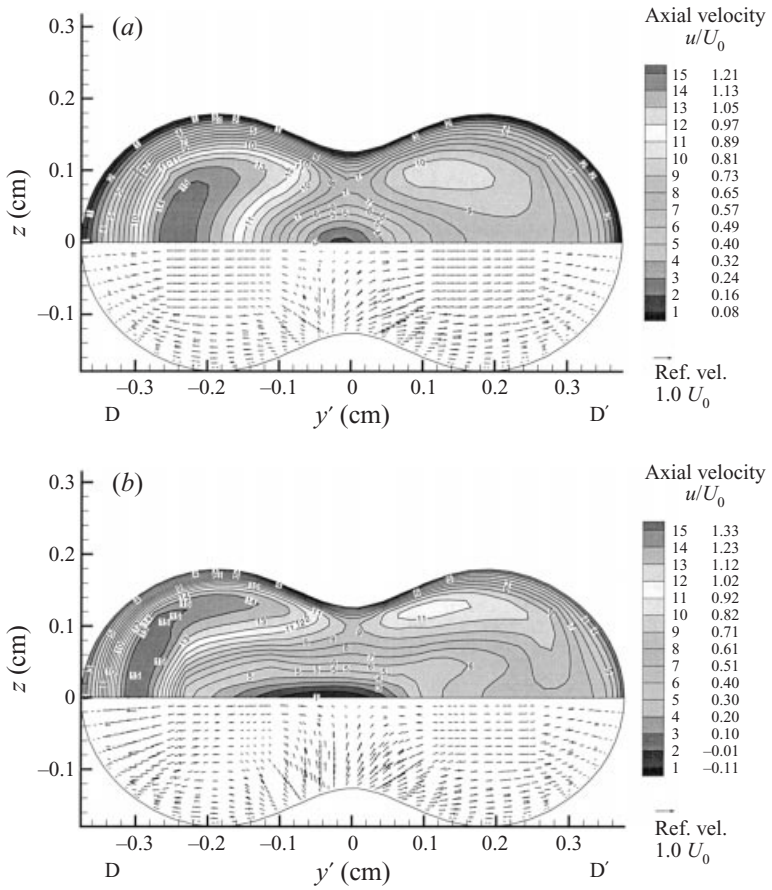


FIGURE 10. As figure 7 but at station D–D′.

the negative axial velocity for the high Reynolds number case. These results have important implications for the local particle deposition results discussed in Part 2 (Comer, Kleinstreuer & Kim 2001). In summary, it explains why, in contrast to the first bifurcation, the particle deposition concentration at the second carina centre is much lower than would be expected based on single bifurcation results. The reason for the low/negative axial velocity at the carina centre can be better understood by observing the secondary velocities in the carinal region and comparing them with that in the first bifurcation (i.e. figure 7*a*, *b*). For the first bifurcation, we see that the carinal ridge has the effect of splitting the flow and pushing it perpendicular to the carinal ridge (i.e. towards the daughter tubes); however, for the second bifurcation the carinal ridge has the effect of squeezing the high-flow region which wrapped around the top/bottom of the bifurcation toward the $z = 0$ symmetry plane. Since the momentum of the off-plane fluid is high, it creates a very low flow region near the carina centre for the low Reynolds number case and reverse flow for the higher Reynolds number flow. While the secondary velocity vector plots for this cross-section indicate that the secondary flow away from the carina is directed toward the outside walls, it should be remembered that the primary flow at this cross-section is aligned with the daughter tube and thus the secondary flow for this cross-section is biased toward the outside of the bifurcations.

https://doi.org/10.1017/S0022112001003809 Published online by Cambridge University Press

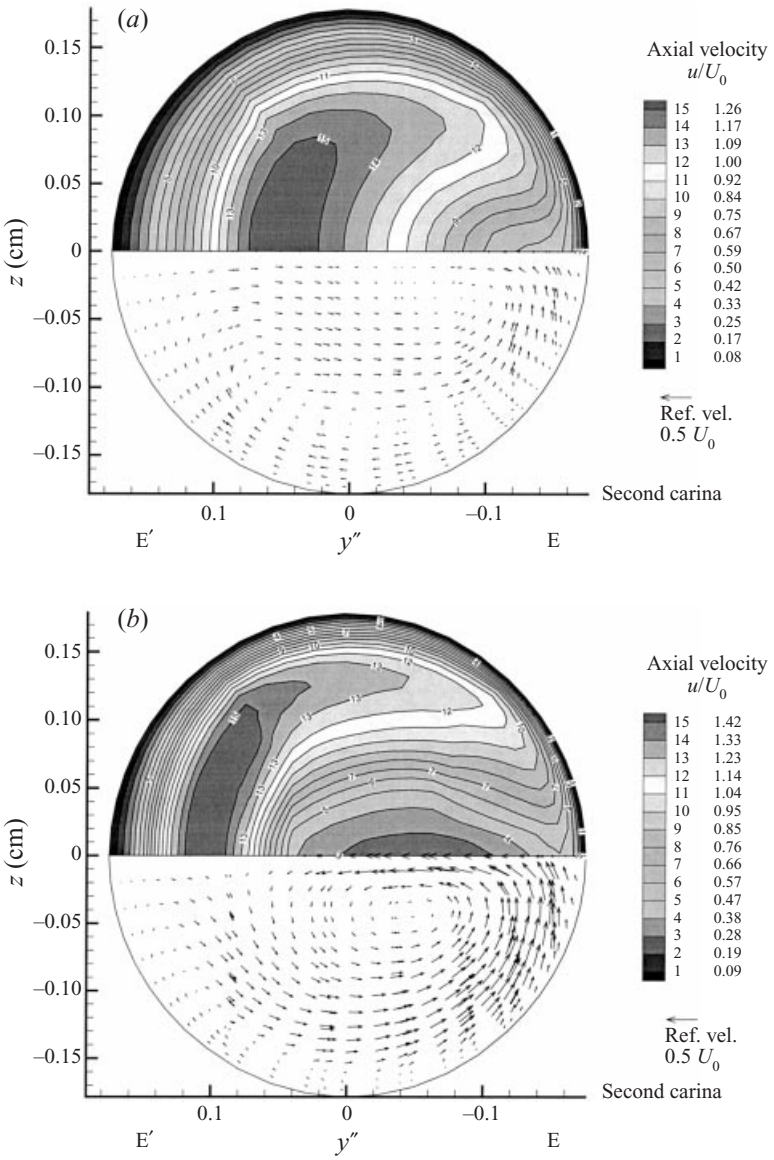


FIGURE 11. As figure 7 but at station E–E′.

Figure 11(*a*, *b*) shows the velocity fields in cross-section E–E′ at the beginning of the 'lower' daughter tube, i.e. inside the second bifurcation. This cross-section corresponds to a bifurcation angle of approximately 21°; thus, the daughter tube is still curving because the total bifurcation angle is 30°. The maximum axial velocity has shifted toward the centre of the daughter tube for the low Reynolds number case. The secondary velocity indicates that the flow in the central portion of the daughter tube moves toward the inside of the second bifurcation, while flow along the inside of the second bifurcation moves down toward the symmetry plane. This effect was described above for section D–D′. For the high Reynolds number case the maximum velocity is wrapped around the top/bottom of the daughter tube, engulfing the slower moving flow as in the previous bifurcation. The secondary velocity for

https://doi.org/10.1017/S0022112001003809 Published online by Cambridge University Press

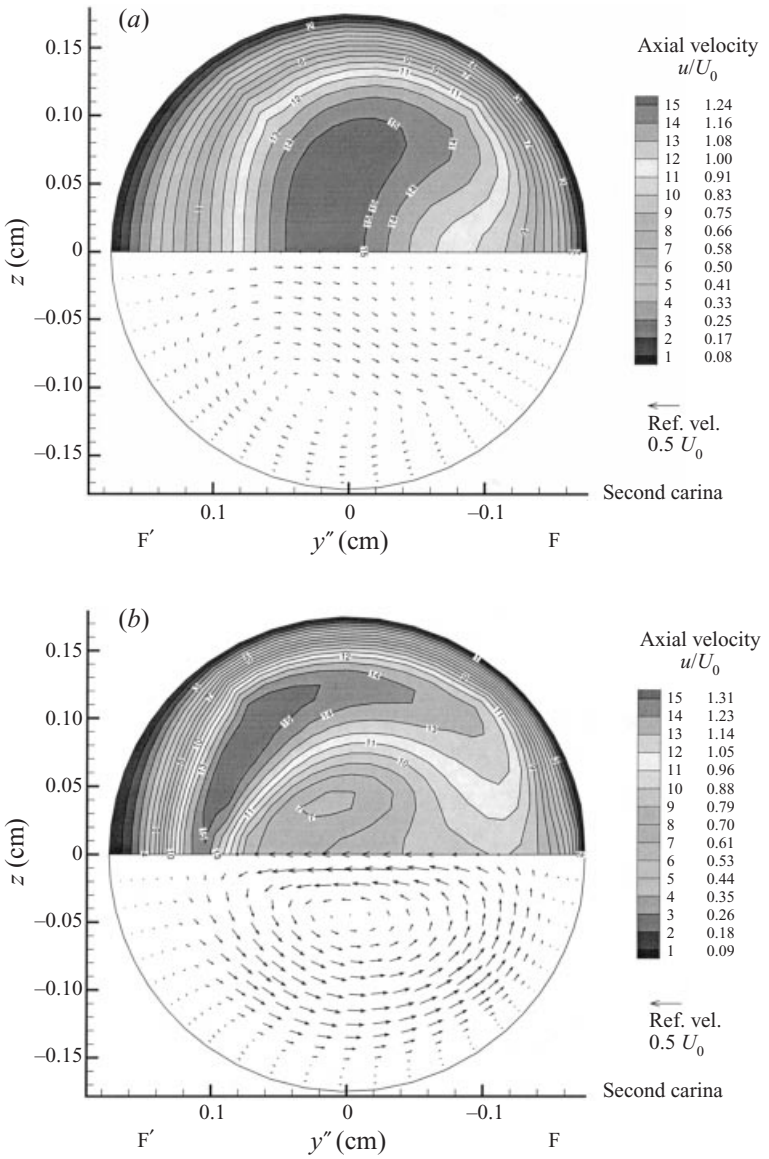


FIGURE 12. As figure 7 but at station F–F′.

this case appears to indicate that the vortex from the first bifurcation persists into the second bifurcation daughter tube. The primary vortex from the first bifurcation appears to be strengthened by the carinal effect. A narrow secondary vortex also appears on the outside of the second bifurcation and extends up along the wall. This weak vortex may be induced by the primary vortex or it could be attributed to the Dean flow effect since the rotation would be toward the outside of curvature, i.e. inside of the second bifurcation. By the Dean flow effect we are referring to the centrifugal acceleration, U^2/R_b, which occurs in curved tubes due to the localized velocity field and the bifurcation curvature, R_b. In summary, the secondary flow field in this domain is a result of multiple interactions: (i) the upstream flow field, (ii) the

https://doi.org/10.1017/S0022112001003809 Published online by Cambridge University Press

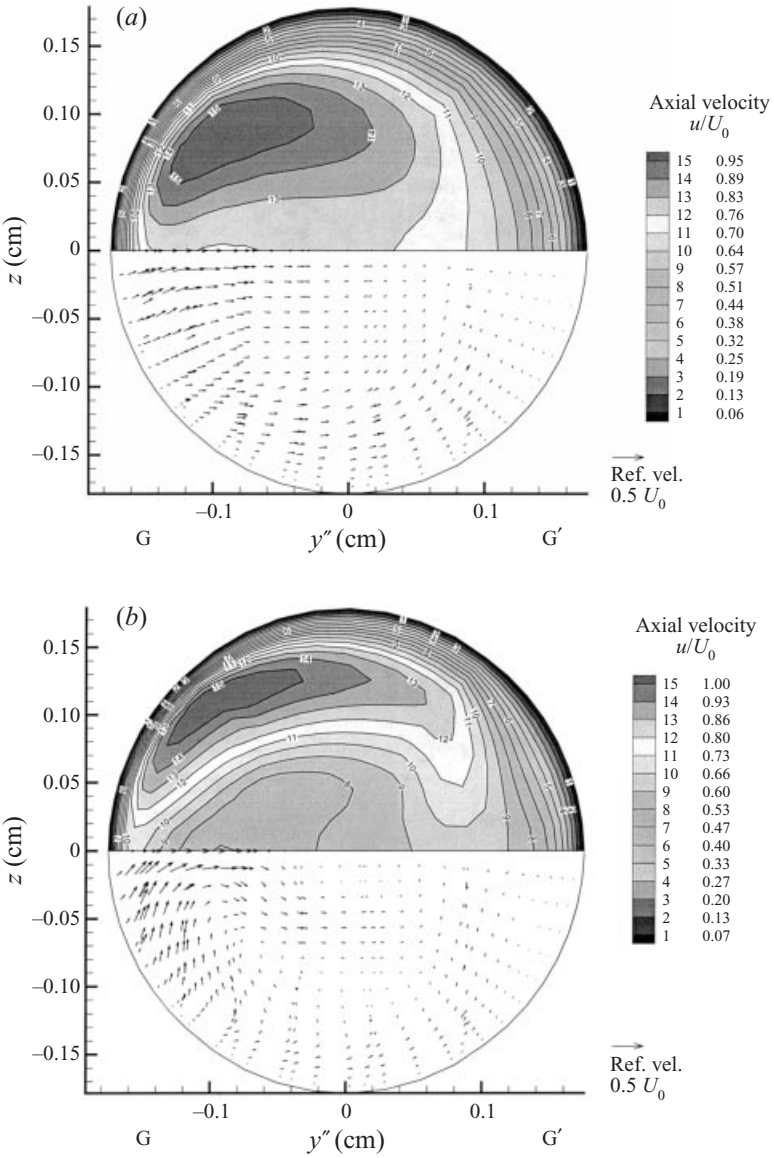


FIGURE 13. As figure 7 but at station G–G′.

bifurcation curvature (i.e. Dean flow effect), and (iii) the effect of the carinal ridge shape.

Figure 12(*a*, *b*) shows the velocity field in cross-section F–F′ at the end of the bifurcation curvature (i.e. bifurcation angle of 30°) for the inside tube. At $Re_{D_1} = 500$, the maximum velocity region has continued to shift back toward the centre of the daughter tube due to the secondary motion. When $Re_{D_1} = 2000$, the highest-axial-velocity fluid has continued to rotate around the top of the daughter tube, lifting off from the symmetry plane. The secondary vortex (see figure 12*a*, *b*) has spread completely around the tube circumference. From this point forward the daughter tubes are straight, thus any curvature effects (i.e. Dean flow effect) will no longer contribute to the secondary motion. As a result of the continued flow development in

https://doi.org/10.1017/S0022112001003809 Published online by Cambridge University Press

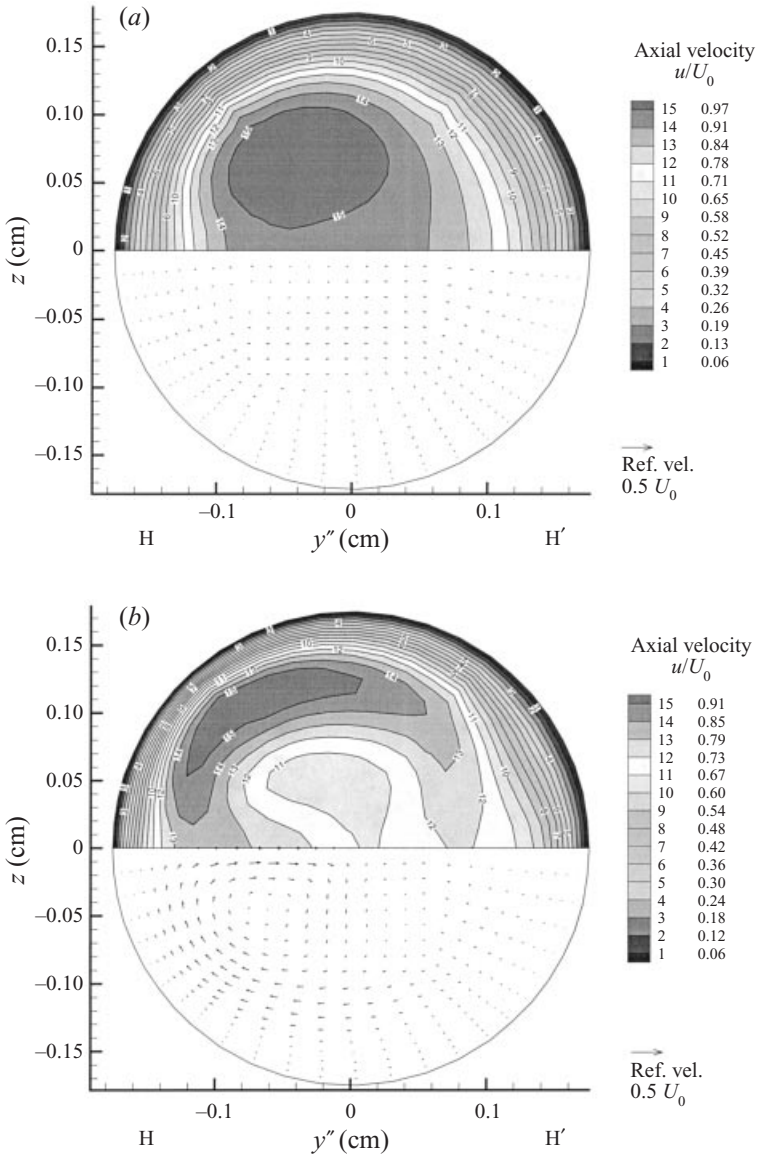


FIGURE 14. As figure 7 but at station H–H′.

the straight 'lower' daughter tube, the maximum velocity region is essentially centred there for the low Reynolds number case (Comer 1998). The rotation of the vortices is such that they would increase the extent of the high-velocity region normal to the symmetry plane. However, the secondary flow effects in the straight tube become negligible. The highest-axial-velocity region for the high Reynolds number case has continued to rotate around until it is located on the inside of the second bifurcation tube. Again, the secondary velocities for the high Reynolds number case persist further down the daughter tube, as would be expected.

Figure 13(*a*, *b*) shows the velocity field in cross-section G–G′ at the beginning of the 'upper' daughter tube, i.e. outside the second bifurcation. As with cross-section E–E′, this cross-section corresponds to a bifurcation angle of approximately 21°. Owing

https://doi.org/10.1017/S0022112001003809 Published online by Cambridge University Press

to the clipping of the high-flow regions described for section D–D′, the maximum axial velocity for both the high and low Reynolds number cases is located off the symmetry plane. The secondary velocity field for both cases clearly shows the effect of the carina flow mentioned earlier. For the low Reynolds number case the secondary flow indicates a general movement away from the bifurcation centre. The high-flow case shows the existence of two small vortices. Of interest is the flow field comparison between the inside and outside bifurcation slices, i.e. E–E′ vs. G–G′. It is readily apparent that the axial and secondary flow through the inside bifurcation tube after the second carina is stronger than that for the outside tube, which follows directly from the high-speed flow travelling along the inside wall.

Figure 14(*a*, *b*) shows the velocity fields in cross-section H–H′ at the end of the bifurcation curvature (i.e. bifurcation angle of 30°) for the outside tube. For $Re_{D_1} = 500$, the maximum-velocity region has continued to shift back toward the centre of the daughter tube. When $Re_{D_1} = 2000$, the highest-axial-velocity flow rotates around the top of the daughter tube toward the inside of the second bifurcation; this is opposite to the rotation in the first bifurcation and the typical Dean flow. However, this rotation may be a continuation of the geometric transition/carina effect shown in section H–H′ or it may be due to a modified Dean flow (inertia effect). The centrifugal acceleration, U^2/R_b, is proportional to the axial velocity, thus it follows that the high-speed region will rotate toward the outside of the curvature (inside of the bifurcation). Since the high-velocity region is located off the symmetry plane, the centrifugal acceleration will act such that the fluid would rotate around the top and bottom of the second daughter tube instead of along the symmetry plane as in normal Dean flow. The secondary vortex is also observed along the top/bottom of the tube. From this point forward the daughter tubes are straight, thus any curvature effects (i.e. Dean-type effect) will no longer contribute to the secondary motion. Comparison between the velocity magnitudes in the inside and outside bifurcation slices, i.e. F–F′ vs. H–H′ can be made. Again, it is readily apparent that the axial and secondary flows through the inside bifurcation tube are stronger than those in the outside tube.

At a location about three tube diameters from the second divider of the outside tube, the maximum-velocity region is centred within the daughter tube and is essentially fully developed for the low Reynolds number case, while the secondary rotation can be considered negligible (Comer 1998). The highest-axial-velocity region for the high Reynolds number case has continued to rotate around until it is located on the inside of the second bifurcation tube. Again, the secondary velocities for the high Reynolds number case persist further down the daughter tube. As previously stated, the secondary circulation of the outside bifurcation tube is considerably weaker than that of the inside tube.

3.2.2. *Planar double bifurcation with sharp carinas*

Figures 15(*a*) and 15(*b*) depict the mid-plane axial velocity contours at $Re_{D_1} = 2000$ in the planar double bifurcation with sharp and rounded carinal ridges, respectively. We can see that the flow fields are quite similar for both configurations. Subtle differences occur in the vicinity of the carinal ridges due to the geometric alterations. The 'round' case has a relatively larger region of instability in the first carinal region compared with the 'sharp' case. The axial flow fields in the first bifurcation shown for configurations with a sharp or rounded ridge (figure 15*a*, *b*) also resemble the flow visualization results obtained by Sudlow, Olson & Schroter (1971, figure 5*a*). The air stream is split at the sharp carina and dispersed to both daughter tubes. In the experiment (Sudlow *et al.* 1971, figure 5*b*; see also Pedley, Schroter & Sudlow

https://doi.org/10.1017/S0022112001003809 Published online by Cambridge University Press

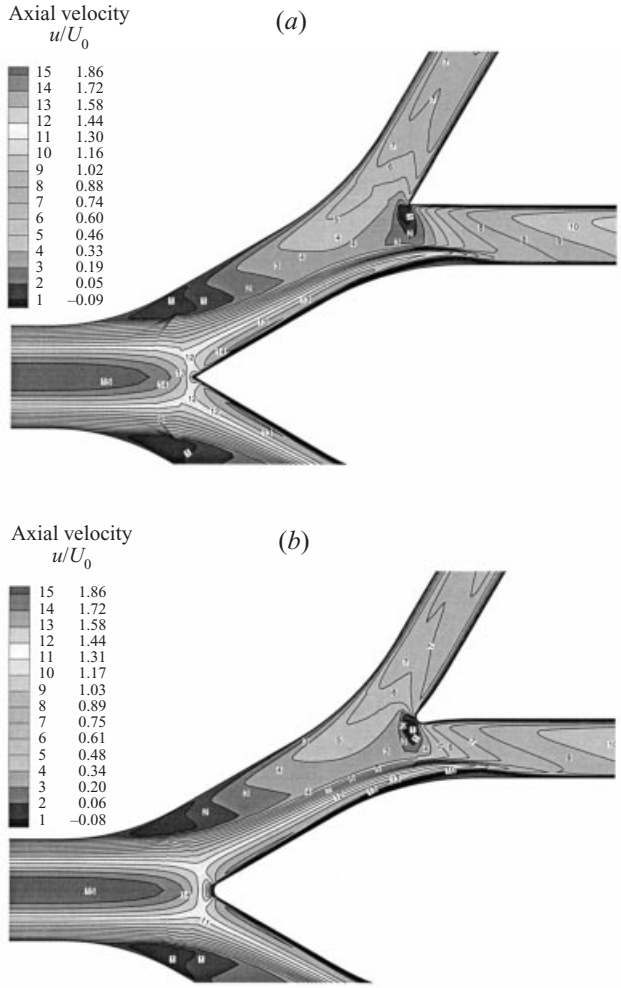


FIGURE 15. Mid-plane axial velocity contours for $Re_{D_1} = 2000$ of planar double bifurcation with (*a*) sharp carinas and (*b*) rounded carinas.

1977), a more complex pattern was observed around a bluff carina where the radius of the edge was much greater than that in the present study, i.e. $r/D \gg 0.1$, where r is the radius of the nose of the flow divider and D the diameter of the daughter branch. The air flow impacts the bluff flow divider, with a portion turned back and outwards to start the secondary motions in the daughter tubes. It should be noted that their flow visualization experiments were conducted using a single-bifurcation model, which is equivalent to the first bifurcation in the present system. There is still no experiment to verify the negative axial flow phenomena upstream of the second carina at $Re_{D_1} = 2000$.

Simulation results also indicated (Kleinstreuer 2000) that the axial velocity contours and secondary velocity at different cross-sections in the configuration with sharp carinas are quite similar to those at the corresponding locations in the bifurcation model with rounded carinas, except in the vicinity of the carinas owing to shape alterations. The magnitude of the velocity just downstream of the carinal ridge for the 'sharp case' is somewhat smaller than that for the 'round case' because of the

https://doi.org/10.1017/S0022112001003809 Published online by Cambridge University Press

smaller blockage effect of the sharp flow divider. The negative axial flow zone which appears in the vicinity of the second carina with a very sharp ridge moves towards the inside daughter tube when compared to the rounded ridge case, which can be attributed to the different squeezing effects of 'very sharp' versus 'round' carinal ridges on the high flow regions.

Noting that the present r/D value of 0.1 is physiologically correct (Horsfield *et al.* 1971) and that the air flow structures do not differ measurably between bifurcations with mildly rounded and very sharp carinal ridges, additional velocity fields are not shown for the sharp ridge case. Furthermore, the following results for the 90° non-planar double bifurcation are only given for the rounded ridge case.

3.2.3. 90° *non-planar double bifurcation*

A characteristic of the 90° non-planar configuration is that the second pair of daughter tubes are turned 90° (see figure 3*c*), as might happen in the upper bronchial tree. Thus deviations in flow patterns when compared with the planar configuration start to appear before the second carinal ridge. Again, owing to symmetry about $z = 0$ only one daughter tube needs to be shown (see figure 5, G–G′ and H–H′). The region downstream of section C–C′ on the bifurcation plane corresponds to the second carinal ridge. For the cases of interest, the high-speed flow travels along the inside wall of the first bifurcation as previously described. Because of the symmetric flow at the second carina, the higher-speed (inertia) fluid travelling along the contracting inside wall follows the carinal ridge past the carina centre, displacing the slower moving fluid along the outside of the second bifurcation carina. The primary difference between the low and high Reynolds number flow is that in the latter case the flow wraps further around the carina.

Figure 16(*a*, *b*) shows the velocity field in cross-section D–D′ just upstream of the carina. The contraction of the left and right surfaces (i.e. the inside and outside surfaces of the first bifurcation) are clearly shown with the deflection of the high-flow region along the inside wall of the second carina. The low Reynolds number case indicates that a low-axial-flow region extends from the outside surface of the first bifurcation toward the carina centre. In the high Reynolds number case this low-flow region extends further into the carina centre, wrapping upward toward the outside of the second bifurcation, and even contains a negative flow region on the outside surface of the first bifurcation. Thus, the high-speed flow which sweeps around the carinal ridge from the inside to the outside has the effect of deflecting the lower-velocity flow coming from the outside of the first daughter tube away from the carinal ridge. Like the planar case, these flow results have important implications for the elucidation of particle deposition patterns. For example, they explain why the particles at the second non-planar carina predominately deposit on the inside half of the carina ridge, since flow (i.e. particles) coming from the outside portion of the first bifurcation is deflected away from the carinal ridge.

Figure 17(*a*, *b*) shows the velocity field in cross-section G–G′ at the beginning of the non-planar daughter tube in the second bifurcation. As was the case for the planar configuration this cross-section corresponds to a bifurcation angle of approximately 21°, thus the daughter tube is still curving to accommodate a total bifurcation angle of 30°. For the planar configurations discussed previously the flow field entering the bifurcation is symmetric about the bifurcation plane (i.e. the prescribed symmetry condition at $z = 0$); however, for the non-planar configuration this is not the case, as discussed previously, and a fully three-dimensional flow field is established at the entrance of the second daughter tube. For the low Reynolds number case the

https://doi.org/10.1017/S0022112001003809 Published online by Cambridge University Press

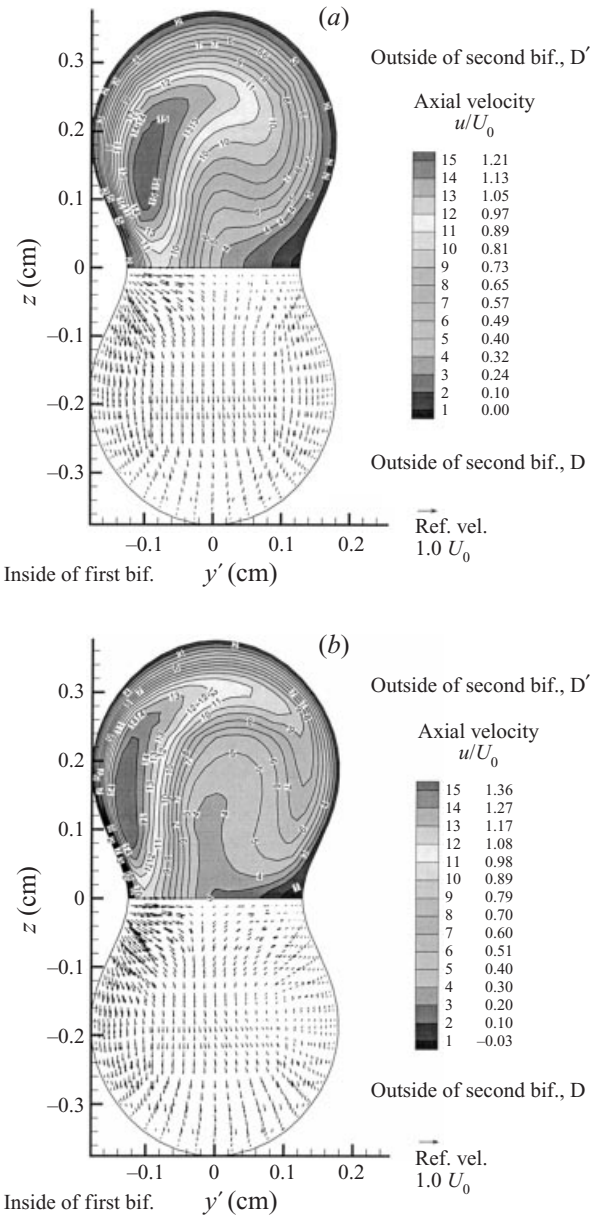


FIGURE 16. Axial velocity contours and secondary velocity vector plots at station D–D′ of non-planar double bifurcation for (*a*) $Re_{D_1} = 500$ and (*b*) $Re_{D_1} = 2000$.

squeezing effect of the second transition region (i.e. carina) has the effect of directing the fluid vertically toward the outside of the second bifurcation ($+z'$) and horizontally wrapping around the bottom (inside, $-z'$) of the second bifurcation. The latter is the same flow feature as described for the cross-section D–D′ (see figure 16*a*, *b*). In the high Reynolds number case the higher-flow region has wrapped almost completely around the slower moving central flow region upstream of the second carina, as discussed for section D–D′. Thus, as the flow enters the second daughter tube there is a high-flow region on the outside of the first bifurcation ($+y'$) which is squeezed or

https://doi.org/10.1017/S0022112001003809 Published online by Cambridge University Press

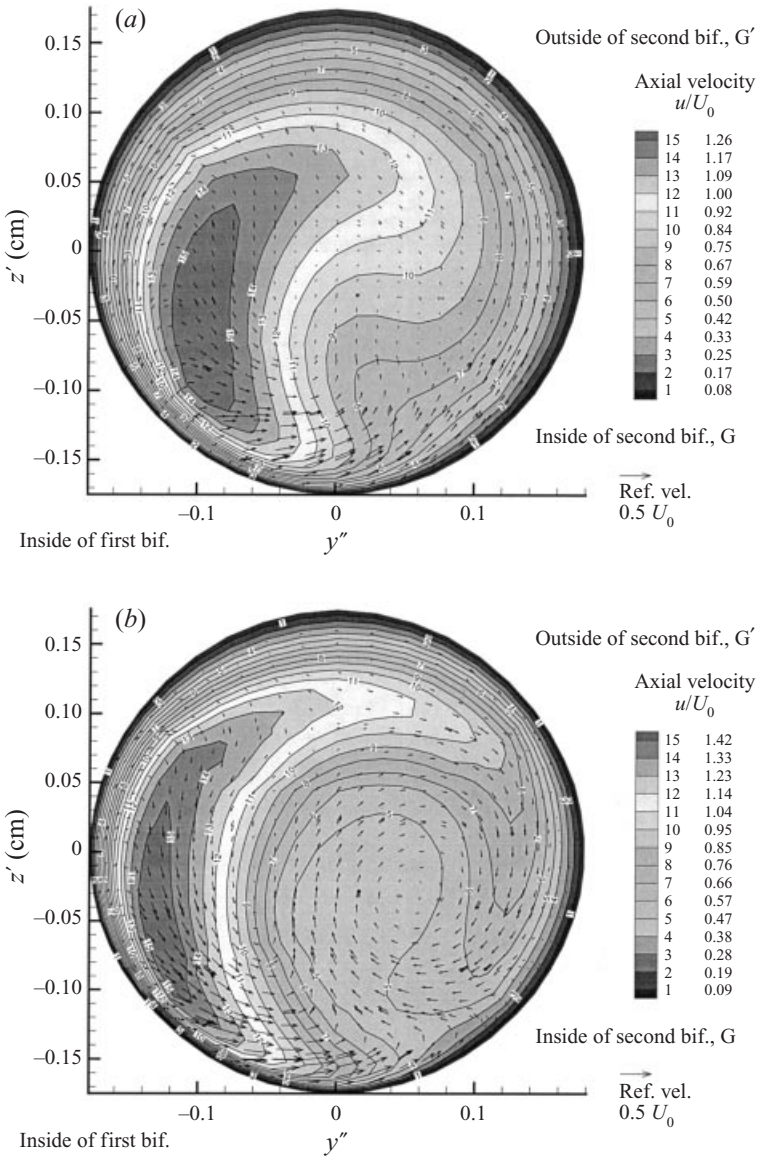


FIGURE 17. As figure 16 but at station G–G′.

funnelled toward the inside of the second bifurcation. This has the effect of opposing the secondary motion wrapping around the bottom (inside, $-z'$) of the second bifurcation; however, the axial flow along the inside wall of the first bifurcation, which contributes to the secondary motion wrapping around the bottom, is much stronger. This results in the smaller vortex (i.e. the opposing vortex) being completely engulfed by the stronger counter-clockwise-rotating vortex. These secondary vortices have the effect of stretching the high-speed axial region around the bottom (inside, $-z'$) and the top (outside, $+z'$) of the second daughter tube, engulfing the low-flow region in the middle of the tube. The strong axial and secondary flow around the inside of the second bifurcation explain the particle deposition patterns shown in Part 2 for the high Reynolds number case. Again, as mentioned for the planar configuration,

https://doi.org/10.1017/S0022112001003809 Published online by Cambridge University Press

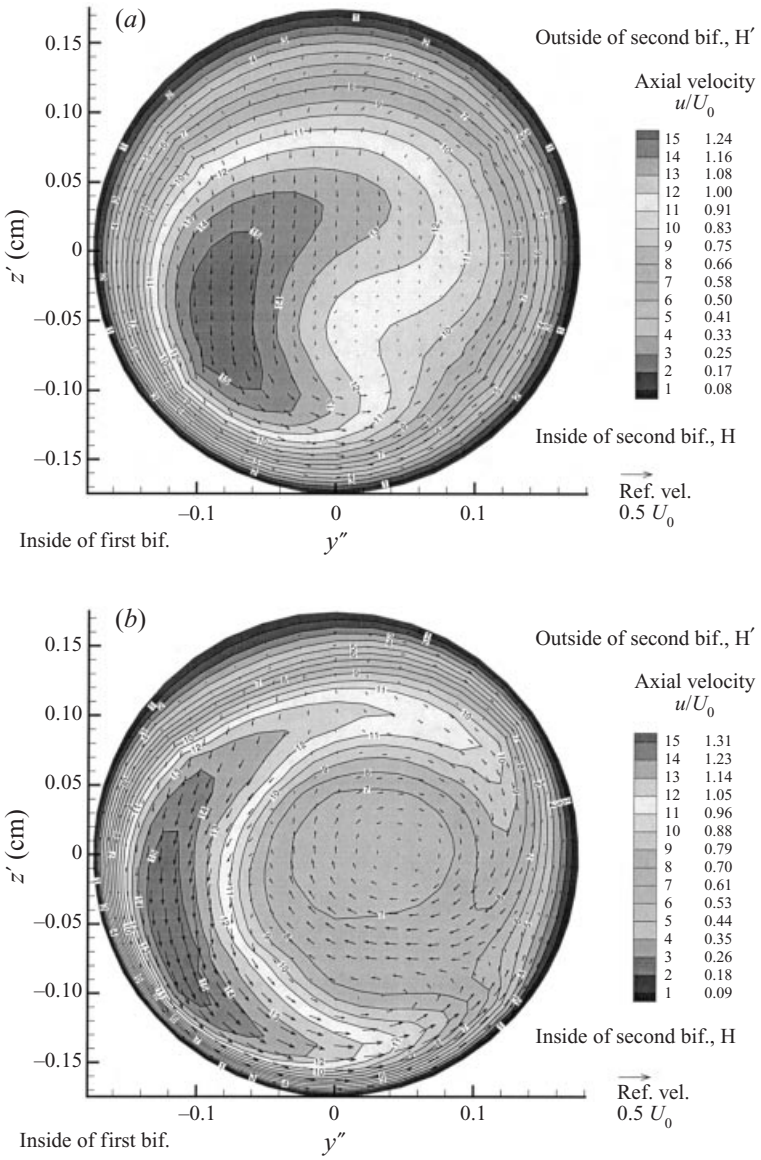


FIGURE 18. As figure 16 but at station H–H′.

the secondary flow field is a result of multiple interactions: (i) the upstream flow field, (ii) the bifurcation curvature (i.e. Dean flow effect) and (iii) the effect of the carinal ridge shape.

Figure 18(*a*, *b*) shows the velocity fields in cross-section H–H′ at the end of the bifurcation curvature (i.e. bifurcation angle of 30°) for the non-planar daughter tube. For the low Reynolds number case the secondary motion continues to move the developing axial flow region toward the inside of the second bifurcation, which is consistent with the Dean flow effect. The region of highest axial flow for the high Reynolds number case is continuing to rotate around the bottom (inside, $-z'$) of the second bifurcation owing to the high secondary motion. The larger counter-clockwise-rotating vortex has completely engulfed the small clockwise-rotating vortex. Since the

https://doi.org/10.1017/S0022112001003809 Published online by Cambridge University Press

remaining portion of the daughter tube is straight, the secondary motion should begin to decay and the flow returns to being uni-axial.

With the flow development downstream of the end of the curved wall, the maximum-axial-velocity region is in the central portion of the daughter tube for the low Reynolds number case; however, due to the secondary rotation it is offset toward the inside of the second bifurcation. The highest-axial-velocity region for the high Reynolds number case has continued to rotate until it is predominately located on the inside of the second bifurcation tube. As expected, the high Reynolds number case has much stronger secondary flow than the low Reynolds number case.

3.3. *Energy dissipation rate and pressure drop*

3.3.1. *Energy dissipation*

In order to predict the pressure drop across the complicated network of bifurcating tubes in the entire lung for a given volumetric flow rate, Pedley, Schroter & Sudlow (1970*a*, *b*, 1971, 1977) and Pedley (1977) proposed a method to calculate the total energy dissipation rate in the bifurcations. Such data sets would be most useful in the development of global algebraic lung models. The calculation was based on their experimental data for a double bifurcation, in which the area ratio of daughter to parent tubes, the branching angles and the local curvatures were different than those in the present model.

The dissipation per unit volume of the incompressible fluid (Φ) at any point can be written as

$$\Phi = \mu \left[2\left(\frac{\partial u}{\partial x}\right)^2 + 2\left(\frac{\partial v}{\partial y}\right)^2 + 2\left(\frac{\partial w}{\partial z}\right)^2 + \left(\frac{\partial v}{\partial x} + \frac{\partial u}{\partial y}\right)^2 + \left(\frac{\partial w}{\partial y} + \frac{\partial v}{\partial z}\right)^2 + \left(\frac{\partial u}{\partial z} + \frac{\partial w}{\partial x}\right)^2 \right]. \quad (3)$$

The dissipation per unit length of the tube at a given station x is then given as

$$\mathscr{D}_1(x) = \oint_A \Phi \mathrm{d}A, \quad (4)$$

where A is the cross-sectional area of the tube, and x is the distance from the flow divider. The total dissipation in a tube between x_1 and x_2 is then

$$\mathscr{D} = \int_{x_1}^{x_2} \mathscr{D}_1(x)\mathrm{d}x. \quad (5)$$

The ratio of $\mathscr{D}_1(x)$ and $\mathscr{D}$ to that in Poiseuille flow can be expressed in terms of dimensionless variables $Y(x)$ and Z:

$$Y(x) = \mathscr{D}_1(x)/(8\pi\mu\bar{U}^2) \quad (6)$$

and

$$Z = \mathscr{D}/[8\pi\mu\bar{U}^2(x_2 - x_1)] \quad (7)$$

where $\bar{U} = (1/A)\oint_A u\mathrm{d}A$.

Following Pedley *et al.* (1977), a junction and its pair of daughter tubes are referred to as a single unit. This consists of the region between two stations: one is at the downstream end of the parent tube before it ceases to be circular (see station 1 of figure 5), and the other is at the downstream end of a daughter tube (station 2). Pedley *et al.* (1970*a*, *b*, 1971, 1977) neglected the viscous dissipation at the junction and in

https://doi.org/10.1017/S0022112001003809 Published online by Cambridge University Press

Case	1				2				3			
Re	1200	900	600	300	720	545	366	190	960	715	474	230
Z	6.13	5.35	4.38	3.04	1.60	1.44	1.27	1.08	1.86	1.69	1.49	1.15
γ	0.23	0.23	0.23	0.23	0.16	0.16	0.17	0.20	0.16	0.17	0.18	0.20

TABLE 3. Energy dissipation rates for different local Reynolds numbers.

the bifurcation zone. (This assumption is discussed below.) Here, we first consider only the viscous dissipation which takes place in the daughter tube between stations 1′ and 2 (figure 5).

As suggested by Pedley *et al.* (1977) and Pedley (1977), the dissipation rate would depend on the Reynolds number and on the distance downstream in the same way as in a regular entrance-length problem. The expression for the dissipation rate in a segment of the tube between stations at distances x_1 and x_2 from the divider is

$$Z = \frac{\gamma \mathrm{Re}^{1/2}}{[(x_1/d)^{1/2} + (x_2/d)^{1/2}]}, \tag{8}$$

where d is the tube diameter, and γ is a constant of proportionality, allowing dissipation to be related to the flow rate. Presumably, its actual value is dependent on the particular geometry.

From (4) and (6) we can obtain the values for $\mathscr{D}_1(x)$ and Y at different positions x. The values of $\mathscr{D}$ are computed from (5) using Simpson's rule using $\mathscr{D}_1(x)$. Finally, the values of Z are obtained from (7), as given in table 3. In this table, case 1 refers to the first daughter tube; cases 2 and 3 represent the outside and inside of the second daughter tube, respectively. With (8), γ can be obtained given the values of Z computed from (7). The values of γ for different cases are also given in table 3. The dissipation rate and pressure drops are different for the planar and non-planar geometries. The presented results are only for the planar geometry.

From table 3, we can see that there is no systematic variation of γ with *Re* for the three cases. However, the difference between the value of γ for case 1 and that for cases 2 and 3 is noticeable. The average value of γ for case 1 is 0.23, while it is 0.17 for cases 2 and 3. Moreover, both these values are much smaller than the one obtained by Pedley *et al.* (1977) from the data set in double bifurcations, where $\bar{\gamma}$ was 0.33. In fact, Pedley *et al.* (1977) also showed that the γ-values in the second bifurcation were uniformly smaller than those in the first bifurcation. Thus, the present simulation results indicate that the greater complexity of the motion after several junctions prevents the complete dominance of an entrance-flow-type boundary layer, as discussed by Pedley *et al.* (1977). This also implies that the local pressure drop predictions in each generation of the entire lung cannot rely on a constant γ-value, e.g. $\bar{\gamma} = 0.33$.

3.3.2. *Pressure drop*

Considering the energy balance for a single unit, i.e. from station 1 to station 2 (see figure 5), the relevant equation is

$$\Delta p = \Delta p_k + \Delta p_v. \tag{9}$$

Here, Δp is the mean static pressure drop, Δp_k the pressure change due to kinetic energy changes, in general negative when the cross-sectional area increases through

https://doi.org/10.1017/S0022112001003809 Published online by Cambridge University Press

Case	*Re*	Δp	$\Delta p_v^{(1)}$	$\Delta p_v^{(2)}$	$\Delta p_v^{(3)}$
1	1200	2.75	5.47	4.57	6.55
	900	1.66	3.33	2.97	4.27
	600	0.92	1.86	1.61	2.32
	300	0.34	0.60	0.57	0.82
2	730	4.01	3.29	4.24	8.25
	547	2.85	2.21	2.80	5.43
	365	1.73	1.27	1.54	2.29
	183	0.49	0.55	0.58	1.12
3	960	2.60	5.71	6.54	12.70
	713	2.29	3.52	4.20	8.16
	475	1.74	1.90	2.27	4.41
	237	0.81	0.68	0.77	1.49

TABLE 4. Pressure drops in daughter tubes (see figure 5) (dimensions in $\mathrm{N\,m^{-2}}$).

the bifurcation, and Δp_v is the pressure drop due to viscous dissipation (also called viscous pressure drop), where

$$\Delta p = \left[\oint_A pu \mathrm{d}A \Big/ \oint_A u \mathrm{d}A \right]_2^1, \tag{10}$$

$$\Delta p_k = \left[\oint_A \tfrac{1}{2}\rho q^2 u \mathrm{d}A \Big/ \oint_A u \mathrm{d}A \right]_1^2, \tag{11}$$

and

$$\Delta p_v = \mathscr{D} \Big/ \oint_A u \mathrm{d}A. \tag{12}$$

Although the pressure drop in one bifurcation is too small to be measured experimentally, it can be obtained from numerical simulation results. Thus the method of predicting static and viscous pressure drops using empirical equations can be examined in the light of the simulated pressure drops. Table 4 lists the pressure drops in different daughter tubes in the present planar double-bifurcation model with rounded carinal ridges at various Reynolds numbers. The values of Δp and Δp_k were obtained from simulations; $\Delta p_v^{(1)}$ was calculated from (9) using simulation data; $\Delta p_v^{(2)}$ and $\Delta p_v^{(3)}$ were computed from values of $\mathscr{D}$ using the following equation (Pedley *et al.* 1977):

$$\mathscr{D} = \bar{\gamma} \left(\frac{d}{l} Re \right)^{1/2} (8\pi\mu \bar{U}^2 l), \tag{13}$$

where l is the length of the tube. In (13), the values of $\bar{\gamma}$ were taken as 0.23 and 0.17 for calculating $\Delta p_v^{(2)}$ in the first and second daughter tube, respectively; and 0.33 (which was used by Pedley *et al.* 1977) for computing $\Delta p_v^{(3)}$ in both bifurcations. The length of the first daughter tube was taken as 0.836 cm and 1.05 cm for the second daughter tube. It is apparent that the predicted viscous pressure drops in generations G4 and G5 using $\bar{\gamma} = 0.33$ are much larger than the simulated values. However, the predicted values of the viscous pressure drop ($\Delta p_v^{(2)}$) agree with the stimulated values, with relative errors below 30%. This indicates that Pedley *et al.*'s method is applicable and useful in predicting viscous dissipation in tubes of bifurcating airway models provided that appropriate $\bar{\gamma}$-values are used for each generation.

https://doi.org/10.1017/S0022112001003809 Published online by Cambridge University Press

Case	1				2			
Re	2000	1500	1000	500	1200	900	600	300
$\Delta p_v^{(1)}$	4.48	2.61	1.23	0.37	4.91	2.88	1.37	0.38

TABLE 5. Simulated viscous pressure drop in the bifurcation zone (around the flow divider) (dimensions in $\mathrm{N\,m^{-2}}$).

Case	*Re*	Δp	$\Delta p_v^{(1)}$	$\Delta p_v^{(2)}$	$\Delta p_v^{(3)}$
1	2000	−2.89	9.95	9.05	6.55
	1500	−1.37	5.94	5.61	4.27
	1000	−0.42	3.09	2.87	2.32
	500	0.038	0.97	0.95	0.82
2	1200	3.94	9.42	10.29	10.48
	900	3.05	5.73	6.38	6.80
	600	2.07	2.95	3.26	3.70
	300	0.93	1.00	1.06	1.31

TABLE 6. Pressure drops in the first and second bifurcation (dimensions in $\mathrm{N\,m^{-2}}$).

Table 5 shows the viscous pressure drop obtained by numerical simulation for selected Reynolds numbers in the bifurcation zone around the flow divider (i.e. from station 1 to station 1′), which had been neglected by Pedley *et al.* (1977). Cases 1 and 2 refer to the viscous pressure drop in the first and second bifurcation zone, respectively. It should be noted that in case 2, averaged values of static pressure and kinetic energy from the inside and outside of the second daughter branch are used to calculate $\Delta p_v^{(1)}$ at station 1′, caused by the difference in local flow rates.

The viscous pressure drop in the bifurcation zones can be described by an empirical equation as follows:

$$\Delta p_v = C_1 Q^a, \tag{14}$$

were Q is the volumetric flow rate ($\mathrm{l\,min^{-1}}$) approaching the flow divider and the coefficients are

Case 1: $C_1 = 0.086$, $a = 1.80$;

Case 2: $C_1 = 0.313$, $a = 1.846$.

Table 6 lists the total simulated static pressure drop Δp and the viscous pressure drop $\Delta p_v^{(1)}$ in one bifurcation (i.e. between stations 1 and 2). The predicted viscous pressure $\Delta p_v^{(2)}$ obtained with the present method (i.e. considering the dissipation in both the bifurcation zone and the daughter tube), and $\Delta p_v^{(3)}$ via Pedley *et al.*'s simplified method are given as well. The meaning of cases 1 and 2 is the same as those in table 5. It is apparent that the predicted viscous pressure drops ($\Delta p_v^{(2)}$) are essentially consistent with the numerically stimulated values ($\Delta p_v^{(1)}$). Compared with the simulated pressure drops, Pedley *et al.*'s approach underestimates the viscous pressure drops for case 1, though it overestimates the viscous pressure drops in the tubes of generation G4. This is because the relatively high viscous dissipation rates around the flow dividers were neglected. In contrast, the viscous pressure drop $\Delta p_v^{(3)}$ for case 2 is consistently overestimated, and approximated to the simulated values, because the overestimation of the viscous pressure in the tube of G5 will cancel the errors caused by neglecting the viscous pressure drop in the bifurcation zone. This

https://doi.org/10.1017/S0022112001003809 Published online by Cambridge University Press

may account for the fact that the overall bronchial pressure drop predicted by Pedley *et al.* (1977) agrees well with some experimental values (Ferris, Mead & Opie 1964). In summary, the overestimated effect of viscous dissipation in the daughter tubes after the trachea using $\bar{\gamma} = 0.33$ in Pedley *et al.*'s model will cancel some errors of neglecting the viscous dissipation in the bifurcation zones.

4. Conclusions

The validated computer analysis of the multi-generational respiratory model provides insight into the complex flow patterns which exist in the human respiratory airways, mainly due to the interactions of upstream flow fields and flow patterns generated by the transition geometries, including changes in cross-sectional areas, wall curvatures, and carinal ridges. These results indicate the underlying mechanism that determines the deposition patterns and local surface concentrations of aerosols, the primary topic of the companion paper (see Part 2, Comer *et al.* 2001). While Weibel's lung model contains realistic tube diameters and lengths, it bifurcates symmetrically and hence may not be fully representative of actual lung casts. Nevertheless, because of its ease of use the model has been, and is being, used by the vast majority of aerosol researchers for direct comparison of experimental and theoretical results. Although most bronchial bifurcations are somewhat asymmetric (Horsfield *et al.* 1971; Phillips & Kaye 1997), some studies have shown that steady inspiratory flow in an asymmetric bifurcation exhibits the main features of the symmetric case (Chang & El Masry 1982; Isabey & Chang 1982; Chang & Menon 1985).

The air flow fields in the planar double-bifurcation models with both rounded and sharp carinal ridges exhibit only subtle differences if the radius of the nose of the flow divider (r), is equal to 0.1 or less of the diameter of the daughter branch (D). Earlier studies have shown that the ratio r/D can vary between zero (for a very sharp divider) and one (for a very blunt flow divider), but in general the r/D ratio is approximately 0.1 or less (Horsfield *et al.* 1971). The complexities of the geometries of actual carinal ridge shapes were clearly displayed with *in vivo* photographs taken by Oho & Amemiya (1980). Their pictures exhibit a wide variety of individual carinal ridge shapes, including sharp wedge-like, blunt, parabolic (rounded), and saddle ones. Hence, the rounded carinas with $r/D = 0.1$ in the present configurations should influence the flow field in a physiologically realistic way. In addition, Martonen, Yang & Xue (1994) also showed that there was not much of a difference in velocity fields between different symmetric carinal ridge shapes, at least in their two-dimensional simulations of single-bifurcation models. Thus the present study of air flow in the double bifurcation with slighted rounded ridges should be a representative case for three-dimensional air flow simulation in multiple bifurcation models. Because of the lack of measurable upstream effects, even at $Re = 500$, single bifurcation models are of interest, but they do not capture most of the significant air flow fields in lung airways. This was achieved with the present double-bifurcation planar and 90° non-planar configurations. As a result, the generality and physical insight of the air flow structures described in this paper instil sufficient confidence to extrapolate the results to more complex bifurcating systems. Indeed, extensions to the current double-bifurcation model are under investigation (Kleinstreuer 2000; Zhang, Kleinstreuer & Kim 2001).

The major differences in flow patterns between the present planar and non-planar models are the following. (i) The flow patterns of both configurations begin to change upstream of the second carina. In the non-planar configuration, the high-axial-flow

https://doi.org/10.1017/S0022112001003809 Published online by Cambridge University Press

region moves toward the inside wall of the second carina, and a low-axial-flow region extends from the outside surface of the second bifurcation toward the carinal centre. The high-speed flow sweeps around the carinal ridge from the inside to the outside and deflects the lower-velocity flow coming from the outside of the first daughter tube away from the carinal ridge. As a result, particles (Part 2) deposit mainly on the inside half of the carinal ridge for non-planar geometries. (ii) In the second daughter tubes of the non-planar configuration, the flow field is not symmetric about the bifurcation plane, and fully three-dimensional flow is established at the 'entrance'. The fluid is directed vertically toward the top of the tube and horizontally wrapped around the bottom. Strong axial and secondary flows are formed near the bottom of the second daughter tube as the flow develops. However, for planar geometries, the maximum-axial-velocity region and the primary vortex stay near the tube centre in most cases.

According to the simulated velocity and pressure fields in the present planar double-bifurcation model representing generations G3–G5 in Weibel's lung model, it is shown that the expression for the energy dissipation rate $\mathscr{D}$ as proposed by Pedley *et al.* (1977) can be successfully employed to predict viscous pressure drops in the daughter tubes with appropriate values of $\bar{\gamma}$. The value of $\bar{\gamma}$ changes with the generation number. In addition to the tubular pressure drops, the energy dissipation in each bifurcation zone has to be accounted for as well. The results, i.e. sequential pressure drops in bifurcating lung airways, are most useful in the development of global algebraic lung models.

REFERENCES

AEA Technology 1997 *CFX-4.2: Solver*. CFX International, Oxfordshire, UK.

Chang, H. K. & El Masry, O. A. 1982 A model study of flow dynamics in human central airways. Part I: Axial velocity profiles. *Respir. Physiol.* **49**, 75–95.

Chang, H. K. & Menon, A. S. 1985 Air flow dynamics in the human airways. In *Aerosols in Medicine. Principles, Diagnosis and Therapy* (ed. F. Moren, M. T. Newhouse & M. B. Dolovich), pp. 77–122. Elsevier.

Comer, J. K. 1998 Computational two-phase flow analyses and applications to gas-liquid and gas-solid flows. PhD Thesis, Mechanical and Aerospace Engineering Department, North Carolina State University, Raleigh, NC.

Comer, J. K., Kleinstreuer, C. & Kim, C. S. 2001 Flow structures and particle deposition patterns in double bifurcation lung models. Part 2. Aerosol transport and deposition. *J. Fluid Mech.* **435**, 55–80.

Farag, A., Hammersley, J., Olson, D. & Ng, T. 1998 Fluid mechanics of a symmetric bifurcation model of the human pulmonary system. *Proc. FEDSM'98: ASME Fluids Engineering Div. Summer Meeting, June 21–25, Washington, DC,* pp. 1–8. ASME FED SM4804.

Ferris, B. G., Mead J. & Opie, L. H. 1964 Partitioning of respiratory flow resistance in man. *J. Appl. Physiol.* **19**, 653–658.

Fox, S. I. 1993 *Human Physiology*, Chap. 15. W. C. Brown Publishers, Dubuque, IA.

Gatlin, B., Cuicchi, C., Hammersley, J., Olson, D., Reddy, R. & Burnside, G. 1995 Computational simulation of steady and oscillating flow in branching tubes. In *Bio-Medical Fluids Engineering*. ASME FED Vol. 212, pp. 1–8.

Gerrity, T. R., Lee, P. S., Hass, F. J., Marinelli, A., Werner, P. & Lourenço, R. V. 1979 Calculated deposition of inhaled particles in the airway generation of normal subjects. *J. Appl. Physiol.* **47**, 867–873.

Hammersley, J. R. & Olson, D. E. 1992 Physical models of the smaller pulmonary airways. *J. Appl. Physiol.* **72**, 2402–2414.

Horsfield, K., Dart, G., Olson, D. E., Filley, G. F. & Cumming, G. 1971 Models of the human bronchial tree. *J. Appl. Physiol.* **31**, 207–217.

https://doi.org/10.1017/S0022112001003809 Published online by Cambridge University Press

Isabey, D. & Chang, H. K. 1982 A model study of flow dynamics in human central airways. Part II: Secondary flow velocities. *Respir. Physiol.* **49**, 97–113.

Kim, C. S., Brown, L. K., Lewars, G. G. & Sackner, M. A. 1983 Deposition of aerosol particles and flow resistance in mathematical and experimental airway models. *J. Appl. Physiol.* **55**, 154–163.

Kim, C. S. & Fisher, D. M. 1999 Deposition characteristics of aerosol particles in successively bifurcating airway models. *Aerosol Sci. Tech.* **31**, 198–220.

Kleinstreuer, C. 2000 Computer simulation of micron-size particle deposition in sequentially branching lung airways. Keynote address, 8 Nov. 2000; *19th AAAR Conference, St. Louis, Missouri.*

Lee, J. W., Goo, J. H. & Chung, M. K. 1996 Characteristics of inertial deposition in a double bifurcation. *J. Aerosol Sci.* **27**, 119–138.

Lonsdale, R. D. 1993 An algebraic multi-grid solver for the Navier Stokes equations on unstructured meshes. *Intl J. Numer. Meth. Heat Fluid Flow* **3**, 3–14.

Martonen, T. B., Yang, Z. & Xue, Z. Q. 1994 Effects of carinal ridge shapes on lung airstreams. *Aerosol Sci. Tech.* **21**, 119–136.

Oho, K. & Amemiya, R. 1980 *Practical Fiberoptic Bronchoscopy*. Igaku-Shoin, Tokyo.

Patankar, S. V. 1983 *Numerical heat Transfer and Fluid Flow*. Hemisphere.

Pedley, T. J. 1977 Pulmonary fluid dynamics. *Ann. Rev. Fluid Mech.* **9**, 229–274.

Pedley, T. J., Schroter, R. C. & Sudlow, M. F. 1970*a* Energy losses and pressure drop in models of human airways. *Respir. Physiol.* **9**, 371–386.

Pedley, T. J., Schroter, R. C. & Sudlow, M. F. 1970*b* The prediction of pressure drop and variation of resistance within the human bronchial airways. *Respir. Physiol.* **9**, 387–405.

Pedley, T. J., Schroter, R. C. & Sudlow, M. F. 1971 Flow and pressure drop in systems of repeatedly branching tubes. *J. Fluid Mech.* **46**, 365–383.

Pedley, T. J., Schroter, R. C. & Sudlow, M. F. 1977 Gas flow and mixing in the airways. In *Bioengineering Aspects of the Lung* (ed. J. B. West). Marcel Dekker.

Phillips, C. G. & Kaye, S. R. 1997 On the asymmetry of bifurcation in the bronchial tree. *Respir. Physiol.* **107**, 85–98.

Schroter, R. C. & Sudlow, M. F. 1969 Flow patterns in models of the human bronchial airways. *Respir. Physiol.* **7**, 341–355.

Snyder, B. & Olson, D. E. 1989 Flow development in a model airway bronchus. *J. Fluid Mech.* **207**, 379–392.

Sudlow, M. F., Olson, D. E. & Schroter, R. C. 1971 Fluid mechanics of bronchial air-flow. In *Inhaled Particles III*. Unwin, London.

Weibel, E. R. 1963 *Morphometry of the Human Lung*. Academic.

Wilquem, F. & Degrez, G. 1997 Numerical modeling of steady inspiratory airflow through a three-generation model of the human central airways. *J. Biomech. Engng* **119**, 59–65.

Zhang, Z., Kleinstreuer, C. & Kim, C. S. 2001 Flow structure and particle transport in a triple bifurcation airway model. *Trans. ASME: J. Fluids Engng* (in press).

Zhao, Y., Brunskill, C. T. & Lieber, B. B. 1997 Inspiratory and expiratory steady flow analysis in a model symmetrically bifurcating airway. *Trans. ASME: J. Biomech. Engng* **119**, 52–65.

Zhao, Y. & Lieber, B. B. 1994 Steady inspiratory flow in a model symmetric bifurcation. *Trans. ASME: J. Biomech. Engng* **116**, 488–496.

https://doi.org/10.1017/S0022112001003809 Published online by Cambridge University Press